Characterization of high nonlinearity in Brillouin amplification in optical fibers with applications in fiber sensing and photonic logic

Daisy Williams,* Xiaoyi Bao, and Liang Chen

Fiber Optics Group, University of Ottawa, Ottawa, Ontario K1N 6N5, Canada
*Corresponding author: dwill087@uOttawa.ca

A highly accurate, fully analytic solution for the continuous wave and the probe wave in Brillouin amplification, in lossless optical fibers, is given. It is experimentally confirmed that the reported analytic solution can account for spectral distortion and pump depletion in the parameter space that is relevant to Brillouin fiber sensor applications, as well as applications in photonic logic. The analytic solutions are valid characterizations of Brillouin amplification in both the low and high nonlinearity regime, for short fiber lengths.   © 2013 Chinese Laser Press

1. INTRODUCTION

Since the discovery of stimulated Brillouin scattering (SBS) in optical fibers, several mathematical models of the pump-probe interaction undergoing SBS in the steady-state regime have emerged, which are valid for pulse lengths greater than the phonon relaxation time [1]. The two-wave interaction is modeled by a system of ordinary differential equations, which in most cases [2,3] has been solved numerically. However, numerical solutions do not lend themselves easily to the high pump wave depletion-related optimization procedures that are essential for applications in strain and temperature sensing. For example, distributed sensing, using erbium-doped fiber amplifiers (EDFAs) and distributed Raman amplifiers [4–6], has the potential to lead to high pump depletion and would require an appropriately accurate solution.

Several attempts have been made to find analytical solutions of this system of equations. The most common is the un-depleted pump approximation (UPA), employed in [7], which imposes the assumption that the pump wave depletion, due to energy transfer between the pump and probe waves, is negligible. The lack of pump wave depletion is a coarse approximation that does not reflect the challenges of fiber sensing techniques.

In [8,9], an analytical solution for a lossless fiber has been attempted without putting limits on the level of depletion. However, this attempt has been only partially successful— the system of ordinary differential equations has been reduced to a transcendental equation, which still had to be solved numerically.

An interesting technique has been used in [1] to find the analytical solutions for a lossy fiber, placing no limits on the level of depletion in the fiber. The system of ordinary differential equations has been reduced to a transcendental equation involving an integral, which, unfortunately, could be evaluated only numerically. As a result, neither intensity distribution along the fiber, nor Brillouin spectra could be expressed analytically.

A variation of the perturbation technique has been used in [10] with the intention of obtaining an analytical solution for a lossy fiber. However, a solution in the zero-approximation with respect to the attenuation constant has been taken from [9], which, as described above, requires the numerical solutions of a transcendental equation. Contrary to the claim in [10], only a hybrid solution has been obtained, which extends the solution in [8] to a lossy fiber, but otherwise has similar limitations.

Thus, previously obtained solutions are numerical with analytical portions, and, therefore, qualify as hybrid solutions. Though the analytical portions provide useful information about intensity distribution along the fiber, they fall short in describing spectral characteristics of the Brillouin amplification conveyed by the transcendental equation. The lack of analytical expressions for Brillouin spectra substantially limits the utility of the hybrid solution [8] for applications, since spectral measurement is a leading technique for strain and temperature sensing. Methods of avoiding systematic errors in distributed fiber sensing are described in [3,11–13] but do not include the correct conditions under which an undesirable effect of spectral distortion occurs in optical fibers, nor how to more accurately obtain a Lorentzian profile for sensing applications.

We propose fully analytic solutions for calculating the distribution of continuous wave (CW) and probe wave (PW) Brillouin intensities and phases, for an arbitrary pump depletion (0%–100%), and an arbitrary range of pump and probe intensities, in fiber lengths of up to a few kilometers. These solutions are valid for expressing the Brillouin spectrum under different depletion conditions, including the spectral distortion effect that occurs for high levels of pump depletion and high probe powers, which has been

confirmed experimentally. Additionally, we propose a 3D parametric model to aid in avoiding the undesirable spectral distortion via limitations of the parameter space that is relevant to Brillouin fiber sensor applications, as well as photonic logic.

2. MODEL

The process of SBS has been studied in a lossless single mode optical fiber, with core radius of $4.1\ \mu m$. Attenuation terms have been neglected due to the short fiber lengths inherent in the model. The configuration is composed of a CW launched into one end and a PW launched into the other end of the optical fiber. The schematic arrangement, and intensity distribution, is shown in Fig. 1 below. The pump wave experiences depletion while the probe wave experiences amplification (gain).

The counter-propagating CW and PW induce density variations of the fiber through electrostriction, creating an acoustic grating, or wave, which participates in the SBS interaction [1]. In the slowly varying amplitude approximation, the steady state interaction between the CW and the PW and an acoustic wave (AW) is described by the following system of equations [9]. The system is deemed to operate in the steady-state regime with pulse lengths greater than 10 ns:

$$\frac{\partial A_1}{\partial z} = \frac{i\omega_1 \gamma_e}{2nc\rho_0} \rho_1 A_2, \tag{1.1}$$

$$\frac{\partial A_2}{\partial z} = \frac{i\omega_2 \gamma_e}{2nc\rho_0} \rho_1^* A_1, \tag{1.2}$$

$$(\Omega_B^2 - \Omega_1^2 - i\Omega_1 \Gamma_B)\rho_1 = \frac{\gamma_e \omega_1^2 n^2}{\pi c^2} A_1 A_2^*, \tag{1.3}$$

where $\Omega_1 = \omega_1 - \omega_2$ is the angular frequency of the AW caused by the interaction of CW and PW, A_1 is the complex amplitude of the CW, A_2 is the complex amplitude of the PW, ρ_1 is the complex amplitude of the AW caused by the interaction of CW and PW, c is the speed of light, ρ_0 is the density of the fiber, γ_e is the electrostrictive constant, z is the coordinate along the fiber, n is the index of refraction of the fiber, v is the speed of sound in the fiber, Γ_B is the Brillouin linewidth, Ω_B is the Brillouin frequency defined as $\Omega_B = 2nv\omega_1/c$, where ω_1 is the angular frequency of the CW, and ω_2 is the angular frequency of the PW.

In the above arrangement, the PW input parameters are known only at the beginning of the fiber, i.e., at $z = 0$. Correspondingly, the CW input parameters are known only at the end of the fiber, i.e., at $z = L$, where L is the length of the fiber. Therefore, the boundary conditions for system (1) are as follows:

$$|A_1(L)|^2 = A_{10}^2; \qquad |A_2(0)|^2 = A_{20}^2, \tag{2}$$

where A_{10}^2 and A_{20}^2 are known squared absolute values of the complex amplitudes A_1 and A_2, respectively.

The goal is to find analytical expressions for the intensities of the CW and PW. In the dimensionless notation, the system (1) becomes

$$\frac{dY_1}{dl} = \beta_1 \cdot Y_1 Y_2, \tag{3.1}$$

$$\frac{dY_2}{dl} = \beta_3 \cdot Y_1 Y_2, \tag{3.2}$$

$$\left|\frac{\rho_1}{\rho_0}\right|^2 = \beta_5 \cdot Y_1 Y_2, \tag{3.3}$$

with corresponding boundary conditions

$$Y_1(1) = 1; \qquad Y_2(0) = 1. \tag{4}$$

The dimensionless variables $l = (z/L)$, $Y_1 = (I_1/I_{10})$, and $Y_2 = (I_2/I_{20})$ have been introduced to derive the system (3), as well as the following β-coefficients:

$$\beta_1 = \frac{2\gamma_e^2 k^2 \omega_1 I_{20} L}{n^2 c^2 \rho_0 \Omega_1 \Gamma_B} \cdot \frac{1}{1 + \xi^2}, \tag{5.1}$$

$$\beta_3 = \frac{2\gamma_e^2 k^2 \omega_2 I_{10} L}{n^2 c^2 \rho_0 \Omega_1 \Gamma_B} \cdot \frac{1}{1 + \xi^2}, \tag{5.2}$$

$$\beta_5 = \left(\frac{2\gamma_e^2 k^2}{nc\rho_0 \Omega_1 \Gamma_B}\right)^2 \cdot \frac{1}{1 + \xi^2} \cdot I_{10} I_{20}, \tag{5.3}$$

$$\xi = \frac{\Omega_B^2 - \Omega_1^2}{\Omega_1 \Gamma_B}, \tag{6}$$

where L is fiber length, I_1 is CW intensity, I_{10} is initial CW intensity, I_2 is PW intensity, and I_{20} is initial PW intensity.

3. SOLUTION

The method used to obtain the dimensionless intensities Y_1 and Y_2 yields the following result for the dimensionless intensities of the CW and PW waves:

$$Y_1(l) = \frac{Y_1(0) - \frac{\beta_1}{\beta_3}}{1 - \frac{\beta_1}{\beta_3} \cdot \frac{1}{Y_1(0)} \cdot e^{\left(Y_1(0) - \frac{\beta_1}{\beta_3}\right)\cdot \beta_3 \cdot l}}; \qquad Y_1(0) \neq \beta_1/\beta_3, \tag{7}$$

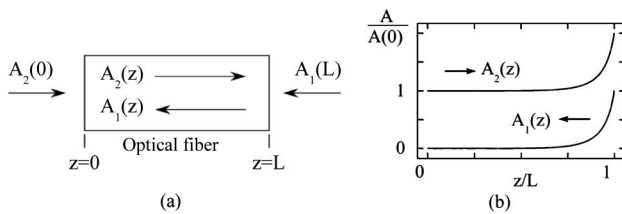$$Y_2(l) = 1 + G_{PW}; \qquad Y_1(0) \neq \beta_1/\beta_3, \tag{8}$$

Fig. 1. (a) Schematic arrangement of SBS in a fiber of length L. Pump and probe configuration: $A_1(z)$—continuous wave, $A_2(z)$—probe wave. (b) Schematic distribution of the pump and probe intensities during SBS.

$$G_{\text{PW}} = \frac{e^{\left(Y_1(0)-\frac{\beta_1}{\beta_3}\right)\cdot\beta_3\cdot l} - 1}{1 - \frac{\beta_1}{\beta_3}\cdot\frac{1}{Y_1(0)}\cdot e^{\left(Y_1(0)-\frac{\beta_1}{\beta_3}\right)\cdot\beta_3\cdot l}}. \tag{9}$$

The expression (9) is the gain the PW experiences. Expression (8), rewritten in terms of dimensional intensities $I_1(z)$ and $I_2(z)$, coincides with the expression for the intensity of the probe wave in [7].

The solution of the system (3) for the intensities (7) and (8) is not complete until an expression for the output intensity $Y_1(0)$ of the CW is determined, which corresponds to the root of the transcendental equation [7], shown in expression (10). As such, previously known solutions, being formally analytical, require the numerical solution of expression (10). Therefore, for all practical purposes, previously obtained solutions are better qualified as hybrid solutions (i.e., partly numerical or graphical and partly analytical):

$$\frac{1}{Y_1(0)-\frac{\beta_1}{\beta_3}}\cdot\ln\left\{\frac{\beta_3}{\beta_1}\cdot Y_1(0)\cdot\left[1+\frac{\beta_1}{\beta_3}-Y_1(0)\right]\right\} - \beta_3 = 0;$$
$$Y_1(0) \neq \beta_1/\beta_3. \tag{10}$$

The analytical solution of $Y_1(0)$ lies in transforming equation (10) into a form suitable for analytical approximation. This form is shown below as expression (11):

$$1 - Y_1(0) - \beta_1\cdot\frac{e^{\beta_3\cdot Y_1(0)-\beta_1} - 1}{\beta_3\cdot Y_1(0)-\beta_1} = 0. \tag{11}$$

The transcendental equation of (11) has a single root "$Y_1(0)$" that depends only on two dimensionless parameters β_1 and β_3 [i.e., $Y_1(0) = x(\beta_1,\beta_3)$]. Additionally, this root falls within the range [0,1], which represents the range of possible dimensionless output intensities of the CW, giving it a physical significance.

Using Eq. (8), we get the following expression for the output intensity of the PW, assuming $Y_1(0)$ is known:

$$Y_2(1) = 1 + \frac{\beta_3}{\beta_1}[1 - Y_1(0)]. \tag{12}$$

4. ANALYTIC SOLUTIONS

Fully analytic expressions (7) and (8) can only be complete when an analytic expression for $Y_1(0)$ is found. Since we are looking for a solution placing no limits on $Y_1(0)$, let us expand the LHS of the equation (11) into a MacLauren series with respect to the variable β_3. If we define, for convenience, $x = Y_1(0)$ and

$$F(\beta_1,\beta_3,x) = 1 - x - \beta_1\cdot\frac{e^{\beta_3\cdot x-\beta_1} - 1}{\beta_3\cdot x-\beta_1},$$

then the corresponding MacLauren series is

$$F(\beta_1,\beta_3,x) = e^{\beta_1} - x - e^{-\beta_1}\sum_{n=1}^{\infty} C_n\cdot x^n\cdot\beta_3^n.$$

Thus, Eq. (11) takes a form suitable for finding approximate analytical solutions:

$$e^{\beta_1} - x - e^{-\beta_1}\sum_{n=1}^{\infty} C_n\cdot x^n\cdot\beta_3^n = 0. \tag{13}$$

A. Linear Approximation
Keeping only linear terms in Eq. (13), we yield the simplest approximation as follows:

$$x = \frac{\beta_1}{(\beta_1+\beta_3)\cdot e^{\beta_1} - \beta_3\cdot(1+\beta_1)}. \tag{14}$$

If better accuracy is required, the quadratic approximation is in order.

B. Quadratic Approximation
Keeping β_3^2 terms in (13), and after some tedious algebra, we yield the next approximation as follows:

$$x = x_{\text{linear}}\cdot\frac{1}{\frac{1}{2} + \sqrt{\frac{1}{4} + x_{\text{linear}}^2\cdot\beta_3^2\cdot\frac{e^{\beta_1}-1-\beta_1-\frac{1}{2}\beta_1^2}{\beta_1^2}}}, \tag{15}$$

where x_{linear} is the output intensity of the CW in the linear approximation, defined in Eq. (14). In a similar way, one can also get the cubic and quartic approximations, which we do not show here due to their complexity.

5. RELATIVE ERROR
To gauge the accuracy of our analytical solutions (14) and (15), we compare them to the numerically calculated solution for the output dimensionless CW intensity. The transcendental Eq. (11) easily lends itself to numerical solution with the use of standard methods of computational physics.

A. Linear Approximation
The relative error is less than 33% in the worst case, on the interval $0 < \beta_1 < 25.4$, $0 < \beta_3 < 6.4$, as it is shown in Fig. 2 below.
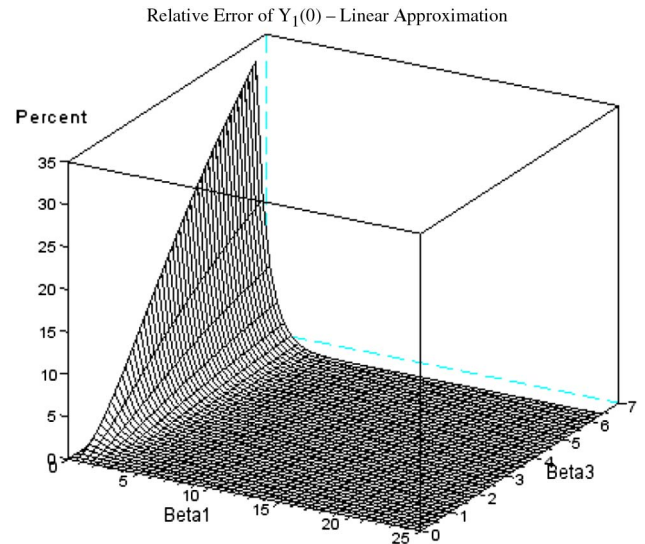

Fig. 2. Relative error of linear approximation of 3D parametric model of output CW. $L = 1000$ m, $0 < P_{\text{pump}} < 10$ mW, $0 < P_{\text{probe}} < 40$ mW.

B. Quadratic Approximation

The relative error of the quadratic approximation is shown in Fig. 3 below.

The relative error of the quadratic approximation is 6.5% in the worst case, which is more than three times smaller than the relative error given by the linear approximation.

Notice, however, that except for a limited combination of parameters for which there is an increase in relative error, deemed to be the "worst case," the relative error in most of the calculations shown in Figs. 2 and 3 is close to 0%. This confirms the utility of the analytic approximations.

6. 3D PARAMETRIC MODEL

An analytic 3D parametric model, attained by plotting the linear approximation solution as a function of dimensionless parameters β_1 and β_3, is shown in Fig. 4.

As can be seen from Fig. 4, the linear approximation (14) covers the entire range of values of output intensities of the CW [i.e., from weak depletion, to full depletion when $Y_1(0) \sim 0$]. In spite of its simplicity, this 3D parametric model is valid in a wide range of combinations of dimensionless parameters β_1 and β_3.

Using Eq. (12), a similar 3D parametric model for the output probe intensity is calculated and shown below in Fig. 5.

As expected, while the CW experiences depletion, the PW experiences amplification.

7. 3D PARAMETRIC MODEL: SIMILAR AND DISSIMILAR PROCESSES

The 3D parametric model for the output CW intensity allows for the easy interpretation of the effects of pump and pulse powers on the level of CW depletion in the fiber. Parameters of the fiber are described in Figs. 4 and 5, and the range of pump and pulse powers $0 < P_{\text{pump}} < 10$ mW, $0 < P_{\text{probe}} < 40$ mW, correspond to the following range of dimensionless parameters β_1 and β_3: $0 < \beta_1 < 6.4$; $0 < \beta_3 < 25.4$. This power range models CW depletion from 0%–100%, corresponding to $0 < Y_1(0) < 1$
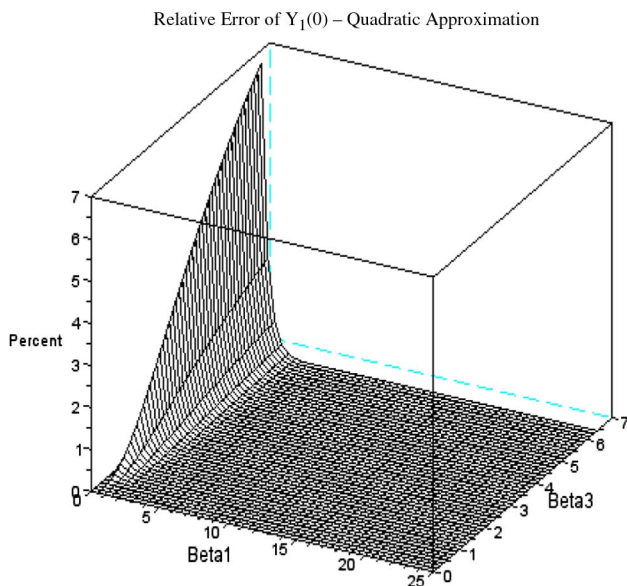

Linearly Approximated output intensity of the CW: $Y_1(0)$

Fig. 4. Linear approximation of 3D parametric model of output CW. Dimensionless output intensity of the CW versus dimensionless parameters β_1 and β_3. $\gamma_e = 0.902$, $v = 5616$ m/s, $n = 1.48$, $\lambda = 1.319$ μm, $\rho_0 = 2.21$ g/cm^3, $\Gamma_B = 0.1$ GHz $L = 1000$ m, $0 < P_{\text{pump}} < 10$ mW, $0 < P_{\text{probe}} < 40$ mW.

in Fig. 4. For example, restricting the range of pulse power to 1.6 mW $< P_{\text{probe}} < 40$ mW yields a depletion of 55%–100%. Further changes in pulse power change the level of depletion accordingly. Being a very versatile model, a change in pulse power, parameters of the fiber, or fiber length would alter the restrictions on β_1 and β_3, therefore allowing for the "picking and choosing" of the preferred level of depletion for the given fiber. For example, in optical fibers it is often preferable to avoid large depletion, which would require a pulse power of <1.6 mW for the parameters given in Figs. 4 and 5.

The study of analytical solutions for the output CW intensity $Y_1(0)$ has led us to notice that certain patterns of similarity exist between various amplification processes in each

Relative Error of $Y_1(0)$ – Quadratic Approximation

Fig. 3. Relative error of quadratic approximation of 3D parametric model of output CW. $L = 1000$ m, $0 < P_{\text{pump}} < 10$ mW, $0 < P_{\text{probe}} < 40$ mW.
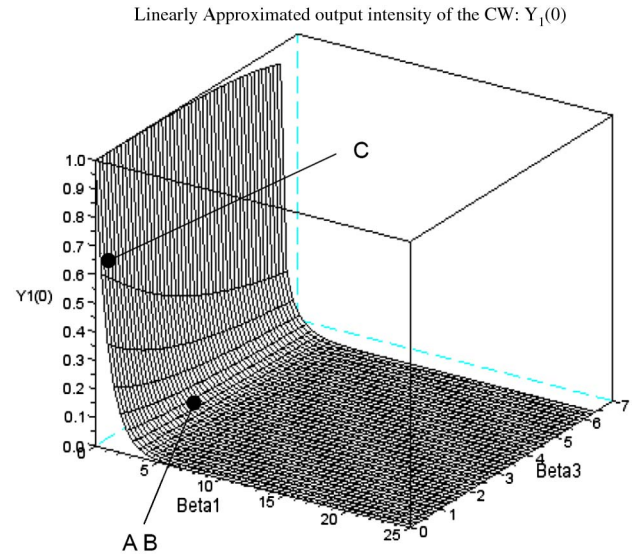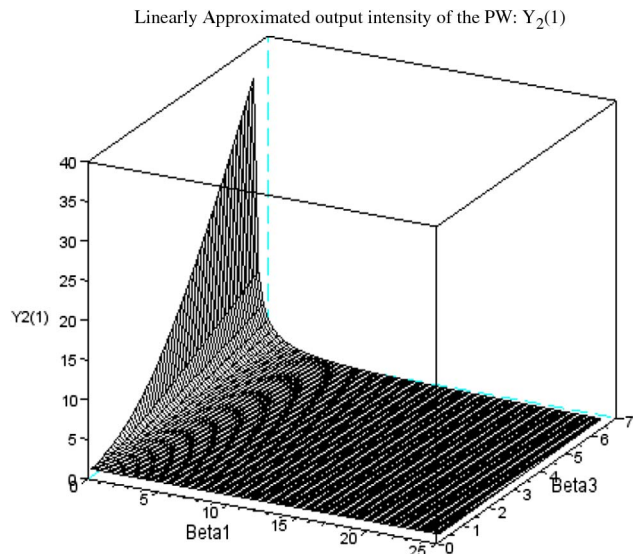

Linearly Approximated output intensity of the PW: $Y_2(1)$

Fig. 5. Linear approximation of 3D parametric model of output PW. Dimensionless output intensity of the PW versus dimensionless parameters β_1 and β_3. $\gamma_e = 0.902$, $v = 5616$ m/s, $n = 1.48$, $\lambda = 1.319$ μm, $\rho_0 = 2.21$ g/cm^3, $\Gamma_B = 0.1$ GHz $L = 1000$ m, $0 < P_{\text{pump}} < 10$ mW, $0 < P_{\text{probe}} < 40$ mW.

regime, even though each process may be described by different combinations of parameters of amplification. Namely, a point on the 3D parametric model, corresponding to a subset of Brillouin amplification processes, determined by the values of the dimensionless parameters β_1 and β_3, is called the *representative point*. Two Brillouin amplification processes are called *similar* if they are characterized by the same representative point. Conversely, two Brillouin amplification processes are called *dissimilar*, if they are characterized by different representative points. The *degree of similarity* between two Brillouin amplification processes A and B is determined by the distance between their representative points, a bigger distance indicating a smaller degree of similarity, and vice versa. Figure [4] above shows an example of two similar and two dissimilar processes. In example 1 below, processes A and B are represented by points A and B, while process C is represented by point C, in Fig. [4].

Example 1.

Similar Processes: $(\beta_1)_A = 3.18$, $(\beta_3)_A = 1.59$, $(\beta_1)_B = 3.18$, $(\beta_3)_B = 1.59$

Process A: $\gamma_e = 0.902$, $\omega_1 = 8.381097 \cdot 10^5$ GHz, $\omega_2 = 8.380692 \cdot 10^5$ GHz, $\Omega_1 = 4.053668 \cdot 10^1$ GHz, $\Omega_B = 4.053668 \cdot 10^1$ GHz, $I_{10} = 12000$ W/cm^2, $I_{20} = 24000$ W/cm^2, $n = 1.45$, $c = 299792.458$ km/s, $v = 5000$ m/s, $\rho_0 = 2.21$ g/cm^3, $\Gamma_B = 0.1$ GHz, $L = 350$ m

Process B: $\gamma_e = 0.8$, $\omega_1 = 8.381097 \cdot 10^5$ GHz, $\omega_2 = 8.380692 \cdot 10^5$ GHz, $\Omega_1 = 4.053668 \cdot 10^1$ GHz, $\Omega_B = 4.053668 \cdot 10^1$ GHz, $I_{10} = 6000$ W/cm^2, $I_{20} = 12000$ W/cm^2, $n = 1.15$, $c = 299792.458$ km/s, $v = 5000$ m/s, $\rho_0 = 1.74$ g/cm^3, $\Gamma_B = 0.1$ GHz, $L = 350$ m

Dissimilar Processes: $(\beta_1)_A = 3.18$, $(\beta_3)_A = 1.59$, $(\beta_1)_C = 4.07 \cdot 10^{-1}$, $(\beta_3)_C = 6.79 \cdot 10^{-2}$

Process A: $\gamma_e = 0.902$, $\omega_1 = 8.381097 \cdot 10^5$ GHz, $\omega_2 = 8.380692 \cdot 10^5$ GHz, $\Omega_1 = 4.053668 \cdot 10^1$ GHz, $\Omega_B = 4.053668 \cdot 10^1$ GHz, $I_{10} = 12000$ W/cm^2, $I_{20} = 24000$ W/cm^2, $n = 1.45$, $c = 299792.458$ km/s, $v = 5000$ m/s, $\rho_0 = 2.21$ g/cm^3, $\Gamma_B = 0.1$ GHz, $L = 350$ m

Process C: $\gamma_e = 0.7$, $\omega_1 = 8.381097 \cdot 10^5$ GHz, $\omega_2 = 8.380692 \cdot 10^5$ GHz, $\Omega_1 = 4.053668 \cdot 10^1$ GHz, $\Omega_B = 4.053668 \cdot 10^1$ GHz, $I_{10} = 8000$ W/cm^2, $I_{20} = 48000$ W/cm^2, $n = 1.53$, $c = 299792.458$ km/s, $v = 5000$ m/s, $\rho_0 = 2.21$ g/cm^3, $\Gamma_B = 0.8$ GHz, $L = 350$ m

8. APPLICATIONS

A. Fiber Sensing

Classification of the Brillouin amplification processes, in terms of their degree of similarity as described above, may have useful applications in the design of various devices based on Brillouin scattering, such as fiber optic sensors. Indeed, a design specification for a device is likely to require that a certain level of output signal be achieved within a certain margin to ensure normal operation of the device. Practice shows that there often exist severe design and technological constraints for many such devices; therefore, though theoretical considerations may suggest a combination of parameters of the Brillouin amplification process that meets the design specification requirements, this theoretical combination may be impractical, expensive, or simply unavailable technologically. In this case, the 3D parametric model would be useful in finding an alternate combination of parameters that is available technologically, and that either meets the requirements of the

design specification or is reasonably close to it. Such a model would allow for the quick and inexpensive attainment of the maximum utility and performance from such a device.

B. Photonic Logic

Another important application is one in photonic logic. In [14], a possible construction of an optical NOT gate utilizing the mechanisms of SBS has been described. To obtain a high switching contrast of 77.6%, such as the one obtained in [14], it is important to find the correct combination of fiber parameters. The initial probe power, P_{probe}, was chosen to be the input signal, and an output CW power, $P_{pump-out}$, was taken to be the output signal of the optical gate. The input CW power was taken to be the reference signal, and was held constant at $P_{pump} = 10$ mW. An input power of 0.1 mW was assigned a logical value of "0," while an input power of 10 mW was assigned a logical value of "1." Output powers of 9.0 and 1.33 mW were obtained for the logical inputs "0" and "1," respectively, yielding the switching contrast of 77.6%. In the configuration described in [14], a SMF-28 fiber was used, of length 350 m, and a 1550 nm laser.

The Brillouin surface can be used to reconstruct this optical gate for any combination of parameters, not only for the ones used in [14]. For example, it is possible to reproduce the optical logic gate of [14] for the SMF-28e fiber, 1310 nm laser, and 1000 m fiber, used in this manuscript, by referring to the Brillouin surface in Fig. [4]. From Fig. [4], it is seen that a reference input CW beam of 10 mW corresponds to $\beta_3 = 6.4$; hence all combinations of parameters must be on the parametric curve corresponding to $\beta_3 = 6.4$. Furthermore, the output CW power of $P_{pump-out} = 1.33$ mW, corresponding to the "0" output, in turn corresponds to $\beta_1 = 0.88$. For the parameters taken in this manuscript, this yields an input probe power of $P_{probe} = 1.4$ mW. Likewise, the output CW power of $P_{1-out} = 9.0$ mW, corresponding to the "1" output, in turn corresponds to $\beta_1 = 0.002$. Again, for the parameters taken in this manuscript, this yields an input probe power of $P_{probe} = 0.003$ mW. Hence, just by looking at the Brillouin surface in Fig. [4], it is possible to find the combination of parameters of the fiber, to recreate the optical logic gate described in [14]. Of course, the 3D parametric model may also be used to construct an optical gate with a higher switching contrast than the one disclosed in [14], or for different, more practical, input powers.

9. SPECTRAL CHARACTERISTICS

A. Analytical Expressions

The starting point in the analysis of analytical expressions for Brillouin output spectra is the previously derived expressions for the output intensities of the CW: $x(\beta_1, \beta_3)$, expressed in Eq. ([14]), and the PW: $\mu(\beta_1, \beta_3)$, expressed in Eq. ([12]). Denoting $x = Y_1(0)$ and $\mu = Y_2(1)$, the following standard approximations are made:

$$\frac{\Omega_B}{\Omega_1} \approx 1; \qquad \frac{\omega_2}{\omega_2} \approx 1; \qquad \Omega_B + \Omega_1 \approx 2\Omega_B. \qquad (16)$$

With these approximations in mind, we yield, instead of ([14]), much simpler expressions:

$$x(\xi) = \frac{b}{(1+b) \cdot e^{\beta_1(\xi)} - 1 - \beta_1(\xi)}, \qquad (17)$$

$$\mu(\xi) = 1 + \frac{1}{b} - \frac{1}{(1+b) \cdot e^{\beta_1(\xi)} - 1 - \beta_1(\xi)}, \qquad (18)$$

where $b = (I_{10}/I_{20})$, $\xi \approx (\Omega_B - \Omega_1)/(1/2)\Gamma_B$.
   And

$$\beta_1(\xi) = \frac{\beta_{10}}{1 + \xi^2}; \qquad \beta_3(\xi) = \frac{\beta_{30}}{1 + \xi^2};$$

$$\beta_{10} = \frac{2\gamma_e^2 k_{air}^2 I_{20} L}{c\rho_0 \Gamma_B \Omega_B}; \qquad \beta_{30} = \frac{2\gamma_e^2 k_{air}^2 I_{10} L}{c\rho_0 \Gamma_B \Omega_B};$$

$$x_0 = x(0) = \frac{b}{(1+b) \cdot e^{\beta_{10}} - 1 - \beta_{10}}. \qquad (19)$$

Analytical expressions for the full width at half-maximum (FWHM) of the spectra may also be obtained, valid for 0%–100% nonlinearity. For the simplicity of notation, we introduce $x_0 = x(0)$, $\mu_0 = \mu(0)$ and recall that $b = \beta_{10}/\beta_{30}$:

FWHM

$$= 2\sqrt{\beta_{10}\frac{1+x_0}{1-x_0}\left(\frac{1}{2} + \frac{1}{2}\sqrt{1 + 2\frac{1+b}{b}\frac{1-x_0}{1+x_0}}\right) - 1} \quad \text{(units of } \Gamma_B\text{)}.$$

$$(20)$$

Using the expressions (7) and (8), we are able to describe the behavior of the CW and PW at every coordinate inside the fiber, and the corresponding output intensity spectra obtained from expressions (17) and (18) above.

   Looking at the probe wave spectrum in Fig. 6, we can see that spectral distortion occurs with increasing probe wave power. Energy is transferred from the pump (higher frequency) to the probe wave (lower frequency). A strong probe
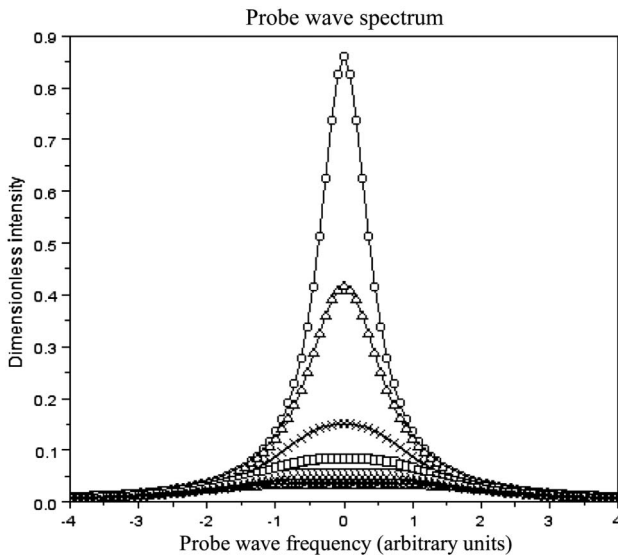
signal can induce pump depletion [15], since it causes the pump to transfer more energy. However, since $P_{CW} < P_{PW}$, saturation effects occur because there is not enough energy supplied by the pump.

   To better demonstrate the correlation between pump depletion and probe spectrum distortion, the Ratio = FWHM/G_{PW} is plotted versus pump depletion in Fig. 7 for various probe powers, where FWHM is the full width at half-maximum of the probe spectrum from expression (20), and G_{PW} is the gain of the probe wave from expression (9). The more distorted the probe spectrum, the higher its ratio value will be. Depletion of the pump was calculated using expression (7).

   As can be seen from Fig. 7, the stronger the probe power, the greater the pump depletion. Consequently, the spectral distortion of the probe spectrum is higher (higher ratio). The Lorentzian shape of the spectrum then becomes flattened and the FWHM increases, as saturation effects begin to become prominent. As such, an output Lorentzian probe wave spectrum (low ratio) is an *indication* of low pump depletion, while an increase in spectral distortion (high ratio) is symptomatic of an increase in pump depletion and saturation effects.

   Pump depletion is detrimental in the field of fiber-optic sensing devices, since it causes a deviation of the peak frequency of the recorded spectrum from the local Brillouin frequency shift, resulting in a systematic error in temperature/strain evaluation [15]. Hence, a Lorentzian probe spectral shape is desired to ensure minimal pump depletion. It is possible to use the 3D parametric surface to avoid parameter combinations, which would lead to such a spectral distortion effect and, instead, choose parameter combinations that would yield an approximate Lorentzian profile. This will be described in more detail in Section 9.B.

B. Transition to a Lorentzian Spectra (Curvature)
As can be seen from Section 9.A, in the nonlinear case, the general expression for the probe wave spectrum (18) does not represent a Lorentzian profile. However, it can be seen from Fig. 6, as well as experimental results (Fig. 10 below), that for certain combinations of parameters, the output PW spectrum is very close, if not indistinguishable, to the Lorentzian spectrum. In this section we will determine the
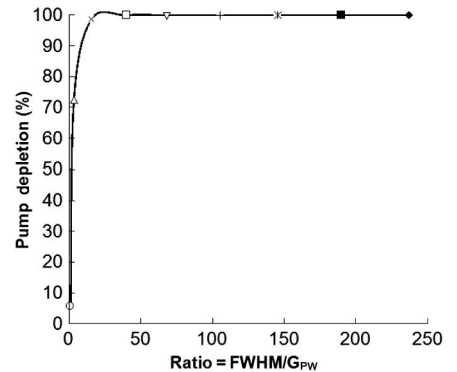

Fig. 6.   Analytical results, normalized intensity units. P_{PW} (mW) = ○ 0.01; △ 1.8; × 6.6; □ 12.1; ▽ 17.1; + 22.4; * 27.2; --- 31.8; — 36.3. $n = 1.48$, $\gamma_e = 0.902$, $\lambda = 1319$ nm, $\rho_0 = 2.21$ g/cm³, $v = 5616$ m/s, $L = 1000$ m, $\Gamma_B = 0.1$ GHz, $P_{CW} = 1.0$ mW.

Fig. 7.   Pump depletion as a function of probe spectral distortion. P_{PW} (mW) = ○ 0.01; △ 1.8; × 6.6; □ 12.1; ▽ 17.1; + 22.4; * 27.2; ■ 31.8; ◆ 36.3. $n = 1.48$, $\gamma_e = 0.902$, $\lambda = 1319$ nm, $\rho_0 = 2.21$ g/cm³, $v = 5616$ m/s, $L = 1000$ m, $\Gamma_B = 0.1$ GHz, $P_{CW} = 1.0$ mW.

Williams *et al.*

Vol. 2, No. 1 / February 2014 / Photon. Res.   7

conditions, within a given level of tolerance, for which the output CW and PW spectra have a Lorentzian profile.

Since a purely Lorentzian spectrum is characteristic of linear systems, it is expected to occur for small nonlinearities (i.e., for small β_{10}, β_{30}). Expanding the expressions (17) and (18) into a power series with respect to β_{10} and β_{30}, we get the following linear approximations:

$$P(\xi) = -x(\xi) + 1 = -\frac{\beta_{30}}{1 + \xi^2} - \frac{1}{2}\frac{\beta_{30}(\beta_{30} - \beta_{10})}{(1 + \xi^2)^2}\cdots, \quad (21)$$

$$S(\xi) = \mu(\xi) - 1 = \frac{\beta_{10}}{1 + \xi^2} + \frac{1}{2}\frac{\beta_{30}(\beta_{30} - \beta_{10})}{(1 + \xi^2)^2}\cdots. \quad (22)$$

It can be seen from Eqs. (21) and (22) that the first (linear) term is representative of a Lorentzian profile, (while higher terms distort it). Ensuring that these distortions are much smaller than the Lorentzian term, we require that

$$\beta_{10} \ll 1, \qquad \beta_{30} \ll 1. \quad (23)$$

For a nonlinear phenomenon like SBS, the spectral shape inevitably deviates from the Lorentzian profile as either the pump power (β_{30}), or probe power (β_{10}) are increased. It can be seen from Fig. 6 that the spectrum becomes flattened quicker than it widens in the onset of spectral distortions. As such, the sharpness of the spectral tip is more sensitive to changes in the spectral shape, as compared to the FWHM of the spectrum. For this reason, we measure the deviation of the spectral shape from the Lorentzian shape by using the relative deviation of the curvature, C_R, of the distorted spectral tip as compared to the Lorentzian spectral tip, according to the following expression:

$$C_R = \left|\frac{C_{CW} - C_{Lorentz}}{C_{Lorentz}}\right|. \quad (24)$$

Using the standard definition of the curvature of the plain curve, as well as expressions (17) and (18), respectively, we yield the following expressions for the curvatures of the CW and PW, C_{CW} and C_{PW}, respectively:

$$C_{CW} = 2\beta_{10}x_0(\beta_{30}x_0 + 1), \quad (25)$$

$$C_{PW} = -2\beta_{30}x_0(\beta_{30}x_0 + 1), \quad (26)$$

where x_0, β_1 and β_3 are defined in Eq. (19). From expressions (21) and (22), we find the curvature of the corresponding Lorentzian profiles (maximum curvature) for the CW and PW, respectively:

$$C_{Lorentz} = 2\beta_{10} \qquad \text{for the CW,} \quad (27)$$

$$C_{Lorentz} = -2\beta_{30} \qquad \text{for the PW.} \quad (28)$$

Given the tolerance δ, we find the following inequality for a quasi-Lorentzian spectral shape:

$$C_R < \delta. \quad (29)$$

The range of β_1 and β_3 values for which the tolerance does not exceed $\delta = 0.20$ from the Lorentzian curvature is shown in Fig. 8. For clarity, the scales along the β_1 and β_3 axes are different. A tolerance of 20% cannot be achieved for β_1-values exceeding 0.50, corresponding to a power range of $0 < P_{PW} < 0.8$ mW for fiber parameters in Fig. 6, while it is possible to choose any β_3-value, which corresponds to the power range $0 < P_{CW} < 10$ mW, provided it is coupled to the correct β_1-value.

This reflects the current theory in which weak probe powers are usually utilized for sensing applications, since this is the regime in which a Lorentz-like profile may be achieved. As such, fiber and strain measurements (measurements of the probe wave) are best conducted within the β-parameters shown in Fig. 8, provided that other factors, not considered here, do not require otherwise.

10. EXPERIMENT

A. Experimental Setup
The experimental setup is shown in Fig. 9. Two narrow linewidth (3 kHz) fiber lasers operating at 1310 nm are used to provide the pump and probe waves, respectively. The frequency difference is locked by a frequency counter and is automatically swept to cover the Brillouin range. A 12-GHz bandwidth high-speed detector is used to measure the beating signal of the pump and probe waves, providing feedback to the frequency counter to lock their frequency differences. The pump laser is launched into an optical circulator, which passes through into the fiber under test (FUT), which is a 1 km Corning SMF-28e. The probe laser is launched into the FUT, to interact with the pump wave, after which it re-enters the optical circulator.

B. Experimental Results
As can be seen from Fig. 10, the same kind of spectral distortion can be seen in the experimental results as shown in the analytical expression of Fig. 6. For both the experimental and
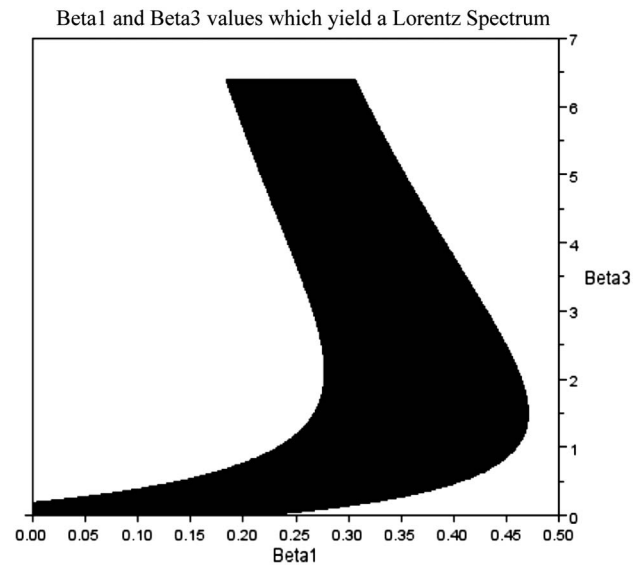
Beta1 and Beta3 values which yield a Lorentz Spectrum

Fig. 8.   Shaded area depicts range of β_1 and β_3 values that yield curvatures within 20% of the Lorentz curvature for both CW and PW spectra.
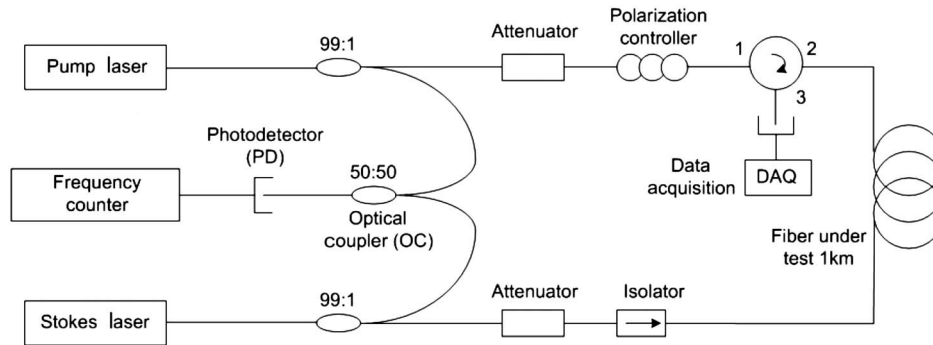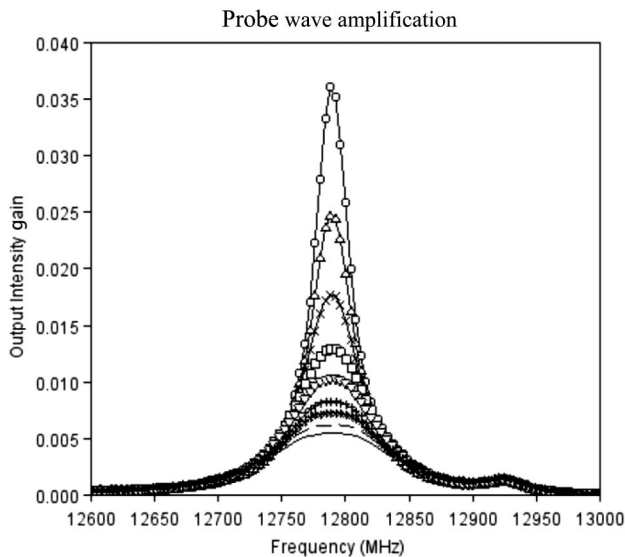
Fig. 9. Experimental setup.

Fig. 10. Experimental results, normalized intensity units. P_{PW} (mW) = ◯ 0.01; △ 1.8; × 6.6; □ 12.1; ▽ 17.1; + 22.4; * 27.2; --- 31.8; — 36.3. $n = 1.48$, $\gamma_e = 0.902$, $\lambda = 1319$ nm, $\rho_0 = 2.21$ g/cm^3, $v = 5616$ m/s, $L = 1000$ m, $\Gamma_B = 0.1$ GHz, $P_{CW} = 1.0$ mW.

theoretical results, the Lorentzian spectrum is maintained for low depletion (i.e., when $P_{PW} \lesssim P_{CW}$), the intensity drop at resonance is progressively more gradual, and the shape becomes flatter. The second, smaller peak seen at 12,925 MHz is a result of second-order Brillouin scattering effects [16], which are not taken into consideration in this paper.

11. CONCLUSION

Accurate analytic expressions have been obtained for Brillouin amplification, describing the intensities of the CW and PW for any coordinate inside the fiber, without any underlying assumptions about the behavior of the pump or probe waves. Among these solutions are (i) the linear approximation which gives a maximum relative error of 33% and (ii) the quadratic approximation which gives a maximum relative error of 6.5%. The relative error for the above analytic solutions quickly decreases to ∼0% for the majority of parameters.

Additionally, analytic solutions for the output pump and probe spectra have been obtained to good accuracy, as well as an expression for the FWHM. These solutions model a spectral distortion effect, which takes place at high pump depletions and high probe powers, and is confirmed experimentally. In sensing applications, the 3D parametric

model may be used to avoid parameter combinations, which yield unwanted spectral distortion effects, such as in distributed sensing where CW depletion is substantial.

The 3D parametric model can also be used to classify the similarity between various Brillouin amplification processes, making it possible to attain the same CW output intensity with a different collection of parameters of the fiber. Such an application has various uses in the field of photonic logic, where reconstruction of optical logic gates for various fiber parameters is required.

REFERENCES

1. R. Boyd, *Nonlinear Optics*, 2nd ed. (Academic, 1992).
2. P. Bayvel and P. M. Radmore, "Solutions of the SBS equations in single mode optical fibers and implications for fibre transmission systems," Electron. Lett. **26**, 434–436 (1990).
3. E. Geinitz, S. Jetschke, U. Röpke, S. Schröter, R. Willsch, and H. Bartelt, "The influence of pulse amplification on distributed fiber-optic Brillouin sensing and a method to compensate for systematic errors," Meas. Sci. Technol. **10**, 112–116 (1999).
4. X. Bao and L. Chen, "Recent progress in distributed fiber optic sensors," Sensors **12**, 8601–8639 (2012).
5. S. L. Zhang and J. J. O'Reilly, "Effect of stimulated Brillouin scattering on distributed erbium-doped fiber amplifier," IEEE Photon. Technol. Lett. **5**, 537–539 (1993).
6. B. Foley, M. L. Dakss, R. W. Davies, and P. Melman, "Gain saturation in fiber Raman amplifiers due to stimulated Brillouin scattering," J. Lightwave Technol. **7**, 2024–2032 (1989).
7. F. S. Gokhan, "Moderate-gain Brillouin amplification: an analytical solution below pump threshold," Opt. Commun. **284**, 4869–4873 (2011).
8. C. L. Tang, "Saturation and spectral characteristics of the Stokes emission in the stimulated Brillouin process," J. Appl. Phys. **37**, 2945–2955 (1966).
9. L. Chen and X. Bao, "Analytical and numerical solutions for steady state stimulated Brillouin scattering in a single-mode fiber," Opt. Commun. **152**, 65–70 (1998).
10. A. Kobyakov, S. Darmanyan, M. Sauer, and D. Chowdhury, "High-gain Brillouin amplification: an analytical approach," Opt. Lett. **31**, 1960–1962 (2006).
11. F. Ravet, *Performance of the Distributed Brillouin Sensor: Benefits and Penalties Due to Pump Depletion*, 1st ed. (University of Ottawa, 2007).
12. T. Horiguchi, K. Shimizu, T. Kurashima, M. Tateda, and Y. Koyamada, "Development of a distributed sensing technique using Brillouin scattering," J. Lightwave Technol. **13**, 1296–1302 (1995).
13. L. Thévenaz and S. F. Mafang, "Depletion in a distributed Brillouin fiber sensor: practical limitation and strategy to avoid it," Proc. SPIE **7753A5**, 1–4 (2011).

Williams *et al.*

Vol. 2, No. 1 / February 2014 / Photon. Res.   9

14. D. Williams, X. Bao, and L. Chen, "All-optical NAND/NOT/AND/ OR logic gates based on combined Brillouin gain and loss in an optical fiber," Appl. Opt. **52**, 3404–3411 (2013).

15. A. Minardo, R. Bernini, L. Zeni, L. Thevenaz, and F. Briffod, "A reconstruction technique for long-range stimulated Brillouin scattering distributed fibre-optic sensors: experimental results," Meas. Sci. Technol. **16**, 900–908 (2005).

16. T. H. Russell and W. B. Roh, "Threshold of second-order stimulated Brillouin scattering in optical fiber," J. Opt. Soc. Am. B **19**, 2341–2345 (2002).